Regular Article – Experimental Physics

Coherent photoproduction of π^0- and η-mesons off ^{7}Li

The Crystal Ball at MAMI, TAPS, and A2 Collaborations

Y. Maghrbi[1], B. Krusche[1,a], J. Ahrens[2], J.R.M. Annand[3], H.J. Arends[2], R. Beck[2,4], V. Bekrenev[5], B. Boillat[1], A. Braghieri[6], D. Branford[7], W.J. Briscoe[8], J. Brudvik[9], S. Cherepnya[10], R.F.B. Codling[3], E.J. Downie[2,3,8], P. Drexler[11], L.V. Fil'kov[10], A. Fix[12], D.I. Glazier[7], R. Gregor[11], E. Heid[2], D. Hornidge[13], I. Jaegle[1], O. Jahn[2], V.L. Kashevarov[10,2], I. Keshelashvili[1], A. Knezevic[14], R. Kondratiev[15], M. Korolija[14], D. Krambrich[2], M. Lang[2,4], V. Lisin[15], K. Livingston[3], S. Lugert[11], I.J.D. MacGregor[3], D.M. Manley[16], M. Martinez[2], J.C. McGeorge[3], D. Mekterovic[14], V. Metag[11], B.M.K. Nefkens[9], A. Nikolaev[2,4], R. Novotny[11], M. Ostrick[2], P. Pedroni[6], F. Pheron[1], A. Polonski[15], S. Prakhov[9], J.W. Price[9], G. Rosner[3], M. Rost[2], T. Rostomyan[6], S. Schadmand[11], S. Schumann[2,4], D. Sober[17], A. Starostin[9], I. Supek[14], C.M. Tarbert[7], A. Thomas[2], M. Unverzagt[2,4], D.P. Watts[7], D. Werthmüller[1], and F. Zehr[1]

[1] Department of Physics, University of Basel, Ch-4056 Basel, Switzerland
[2] Institut für Kernphysik, University of Mainz, D-55099 Mainz, Germany
[3] School of Physics and Astronomy, University of Glasgow, G12 8QQ, UK
[4] Helmholtz-Institut für Strahlen- und Kernphysik, University of Bonn, D-53115 Bonn, Germany
[5] Petersburg Nuclear Physics Institute, RU-188300 Gatchina, Russia
[6] INFN, Sezione di Pavia, I-27100 Pavia, Italy
[7] School of Physics, University of Edinburgh, Edinburgh EH9 3JZ, UK
[8] Center for Nuclear Studies, The George Washington University, Washington, DC 20052, USA
[9] University of California Los Angeles, Los Angeles, California 90095-1547, USA
[10] Lebedev Physical Institute, RU-119991 Moscow, Russia
[11] II. Physikalisches Institut, University of Giessen, D-35392 Giessen, Germany
[12] Laboratory of Mathematical Physics, Tomsk Polytechnic University, Tomsk, Russia
[13] Mount Allison University, Sackville, New Brunswick E4L3B5, Canada
[14] Rudjer Boskovic Institute, HR-10000 Zagreb, Croatia
[15] Institute for Nuclear Research, RU-125047 Moscow, Russia
[16] Kent State University, Kent, Ohio 44242, USA
[17] The Catholic University of America, Washington, DC 20064, USA

Abstract. Coherent photoproduction of π^0-mesons from threshold ($E_{th} \approx 136$ MeV) throughout the Δ-resonance region and of η-mesons close to the production threshold ($E_{th} \approx 570$ MeV for η) has been measured for ^{7}Li nuclei. The experiment was performed using the tagged-photon beam of the Mainz MAMI accelerator with the Crystal Ball and TAPS detectors combined to give an almost 4π solid-angle electromagnetic calorimeter. The reactions were identified by a combined invariant-mass and missing-energy analysis. A comparison of the pion data to plane-wave impulse modelling tests the nuclear mass form factor. So far coherent η production had been only identified for the lightest nuclear systems (^{2}H and ^{3}He). For ^{3}He a large enhancement of the cross section above plane-wave approximations had been reported, indicating the formation of a quasi-bound state. The present Li data for η production agree with a plane-wave approximation. Contrary to ^{3}He, neither a threshold enhancement of the total cross section nor a deviation of the angular distributions from the expected form factor dependence were observed.

1 Introduction

Photoproduction of mesons off nuclei involves in general many different final states of the meson-nucleus system and can contribute to a wide range of topics (see [1] for

an overview). Very interesting for many questions are two limiting cases. In "quasi-free" processes, the reaction involves one specific nucleon, called "participant", which is kicked out of the nucleus, and the rest of the nucleus can be regarded as a "spectator" system that only compensates the momentum of the bound participant. For light

[a] e-mail: Bernd.Krusche@unibas.ch

nuclei, this process is a powerful tool for the study of reactions off quasi-free neutrons [1]; for heavy nuclei it can be used as a testing ground for meson-nucleus interactions and hadron in-medium properties [2].

In "coherent" reactions, ideally the meson is produced via a superposition of the reaction amplitudes from all nucleons and, in the final state, the nucleus remains in its ground state. A similar process in which no nucleon is removed from the nucleus but the nucleus is excited to a higher-lying nuclear state, is sometimes called "incoherent" production. The advantage of the coherent process is the simplicity of the final state; the ground-state properties of nuclei are well under control. This reaction is well suited for the study of the in-medium properties of mesons and nucleon resonances. The undisturbed final state can be easily constructed from the plane-wave impulse approximation and any deviations may be attributed to nuclear effects like meson-nucleus final-state interactions or in-medium modifications of hadron properties. Such programs have been pursued in particular for the study of medium effects on the production and propagation of the Δ-resonance in medium via the coherent $\gamma A \to A\pi^0$ reaction (see, *e.g.*, [3,4]). The same reaction was also exploited for the study of nuclear properties such as nuclear mass form factors [5], and in incoherent production, for nuclear transition form factors [6]. Nuclear form factors in the region of helium and lithium isotopes have gained much new interest in connection with the study of halo nuclei (see, *e.g.*, [7,8]). Coherent pion photoproduction allows the direct study of the nuclear mass distribution because production of π^0 mesons in the Δ-resonance region couples identically to protons and neutrons.

Until now, coherent photoproduction of heavier mesons off nuclei has almost not been investigated since such measurements are very demanding. For mesons like the η, large momenta are transfered to the nucleus, which suppresses the production cross section due to the nuclear form factors. Background from breakup reactions, where the participating nucleon is removed from the nucleus, dominates the production process. This background must be suppressed either by detection of the recoil nucleons or by conditions on the reaction kinematics, demanding detector systems with large solid-angle coverage, large detection efficiency, and excellent energy and angular resolution.

Recently, coherent photoproduction of η-mesons from light nuclei has attracted interest as a tool for the search of so-called η-mesic nuclei [9,10]. The question is whether the strong interaction allows the formation of quasi-bound meson-nucleus states, which would be the ideal system for the study of meson-nucleus interactions. The interaction of low-energy pions with nuclei is too weak for quasi-bound states but the situation is much different for η-mesons. Production of η-mesons in the threshold region is dominated by the excitation of the s-wave $S_{11}(1535)$ resonance [11,12], which couples strongly (branching ratio $\approx 50\%$ [13]) to $N\eta$. As a consequence, the interaction of η-mesons with nuclear matter is important also for very small momenta of the mesons. Typical absorption cross sections are around $30\,\mathrm{mb}$ and are over a wide

range of kinetic energy ($T \approx 1\,\mathrm{MeV}$–$1\,\mathrm{GeV}$) almost independent of T [14,15]. First evidence for an attractive s-wave ηN interaction, which might lead to the formation of quasi-bound states, was reported from coupled-channel analyses of pion-induced η production reactions [16,17] in the 1980s. However, it is still controversially discussed whether the interaction is strong enough to form such states. The original prediction was for nuclei with mass numbers A in the range slightly above 10. However, refined values for the ηN-scattering length extracted from more precise recent η production data extended the discussion to very light nuclei like hydrogen and helium isotopes. (See [10] and references therein for a summary of recent results.)

A much explored experimental approach to identify η-mesic states is the study of the threshold behavior of η production reactions. Quasi-bound states in the vicinity of the production threshold should give rise to an enhancement of the respective cross section over phase-space behavior. Many hadron-induced reactions (see references in [10]) have been studied for this purpose. Interesting threshold effects have been observed for many of them. Particularly strong enhancements were found for the $pd \to \eta^3\mathrm{He}$ [18] and $dp \to \eta^3\mathrm{He}$ reactions [19–21], implying a large $\eta^3\mathrm{He}$ scattering length. If such effects are due to a resonance in the η-nucleus system, they should exist independently of the initial state of the reaction.

Electromagnetic induced reactions, like photoproduction of mesons, offer a very clean way to study the η-nucleus final state, but have small production cross sections, in particular for the coherent process. Photoproduction of η-mesons in the threshold region has been studied for several hydrogen and helium isotopes [9,11,22–27] and these results allowed the characterization of the spin and isospin structure of the relevant transition amplitudes [28]. The reaction is dominated by the excitation of the $S_{11}(1535)$ resonance via the E_{0+} multipole, which involves a spin-flip of the participating nucleon. This means, that coherent η production is practically forbidden for nuclei with spin $J = 0$ ground states. Also for nuclei with non-zero ground-state spins, depending on the nuclear structure, only a fraction of the nucleons (those which can participate in spin-flip transitions) may contribute. Furthermore, the electromagnetic excitation of the $S_{11}(1535)$ resonance is mainly isovector ($A^{IS}_{1/2}/A^{p}_{1/2} \approx 0.1$, where $A^{p}_{1/2}$ is the helicity coupling for the proton and $A^{IS}_{1/2}$ is the isoscalar part of the helicity coupling) [28], so that contributions from protons and neutrons will cancel to a large extent in coherent η production. Together with the large momentum transfers involved, these features lead to very small reaction cross sections.

Only nuclei with ground-state spin J and isospin I different from zero are promising candidates for the observation of the coherent process. Previous experimental results are consistent with this picture. The cross section for coherent production off the deuteron ($J = 1$, $I = 0$) is small [24], (typical values for $\mathrm{d}\sigma/\mathrm{d}\Omega$ are on the order of $10\,\mathrm{nb/sr}$). Only upper limits have been extracted for the $J = I = 0$ nucleus $^4\mathrm{He}$ [26]. The most inter-
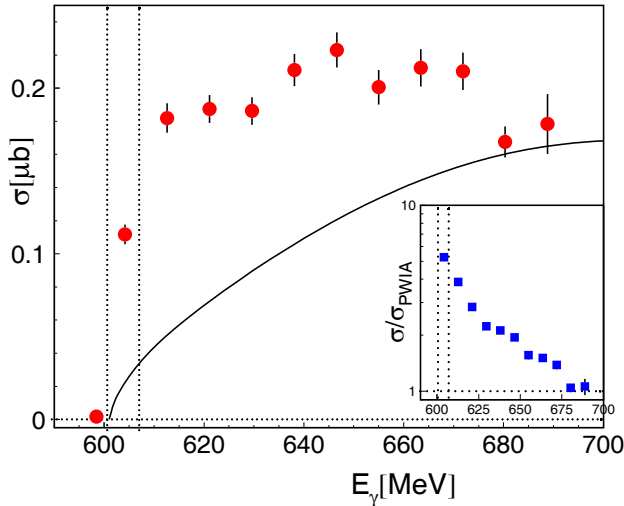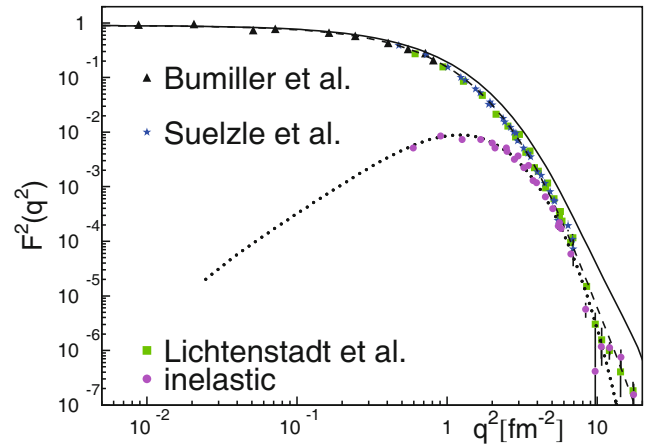
Fig. 1. Total cross section for the $\gamma^3\text{He} \rightarrow \eta^3\text{He}$ reaction [10] compared to plane-wave impulse approximation. Vertical dashed lines indicate coherent and breakup threshold for η production. Insert: ratio of data and impulse approximation.

Fig. 2. Elastic charge form factors from Bumiller *et al.* [31], (black) triangles, Suelzle *et al.* [29], (blue) stars, and Lichtenstadt *et al.*(green) squares. Dashed line: parametrization of form factor F_C. Solid line: form factor F_{C*}. (Magenta) dots: inelastic form factor for 478 keV excitation [32]. Dotted curve: parametrization of inelastic form factor.

esting case studied so far is the $J = I = 1/2$ nucleus ^3He [9,10]. The coherent process was clearly identified. The energy dependence of the total cross section shown in fig. 1 [10] is different from the expectation for reaction phase-space. A strong threshold enhancement relative to the plane-wave impulse approximation (PWIA), similar to the results from hadron-induced reactions [19–21], is observed. The angular distributions close to threshold are more isotropic than expected from the shape of the nuclear form factor [10]. Both observations together have been taken as indication for the formation of a resonant-like meson-nucleus state [9,10].

So far, this is the only isolated case where coherent η-threshold production off nuclei could be studied. Almost nothing is known experimentally about its systematics and the validity of the simple plane-wave impulse approximation used in [9,10]. The present work therefore aimed at the measurement of this reaction from a different light nucleus. Apart from ^3H, the mirror nucleus of ^3He, which, however, is difficult to handle as a target, the lightest stable isotope with nonzero ground-state spin ($J^\pi = 3/2^-$) and isospin ($I = 1/2$) is ^7Li. In the relevant range of momentum transfer its squared form factor [29], which is expected to be proportional to the cross section, is roughly smaller by an order of magnitude compared to ^3He [30]. However, a factor of ≈ 3 in counting statistics may be recovered from the target thickness (number of nuclei/cm^2), making the measurement feasible.

This paper is organized as follows. The assumptions and inputs for the modelling of coherent π^0 and η photoproduction off ^7Li in plane-wave impulse approximation are discussed in sect. 2. The experimental setup is described in sect. 3 and the data analysis, in particular the identification of events from the coherent process, is discussed in sect. 4. The measured cross sections for coherent π^0 and η production are summarized in sect. 5 and compared to the results of the PWIA modelling.

2 Plane-wave impulse approximation

The PWIA of the coherent meson production follows the work of Drechsel *et al.* [3], taking into account the specific features of the $\pi^0 - A$ and $\eta - A$ final states. The main inputs are nuclear form factors and the amplitudes for the elementary meson production reactions off the free nucleon. The elastic charge form factor F_C of ^7Li has been measured with electron scattering over a wide range of momentum transfer q [29,31,32]. Lichtenstadt *et al.* [32] also reported results for the inelastic transition form factor F_{Cx} related to the excitation of the 478 keV state in ^7Li. Since the charge and mass rms radii of ^7Li are similar [7, 33], we can use the charge form factors as basis. However, they include the effects from the charge distribution of the proton. For the meson production reactions we need instead the distribution of point-like nucleons. Therefore, the measured charge form factors must be divided by the proton dipole form factor $F_p^2(q^2)$; the ratios are denoted by F_{C*} and F_{Cx*}. Figure 2 summarizes the charge form factors and their parametrizations used in the PWIA modelling. For the elastic form factor, the parametrization of F_{C*} is also shown. The q dependence of the inelastic form factor F_{Cx} for small values of q is approximated by the model results cited in [32].

The construction of the transition amplitudes starts from the effective total energy $W = \sqrt{s^{\text{eff}}}$ of the incident photon (four-momentum P_γ, laboratory energy E_γ) and an off-shell nucleon (four-momentum P_N) with three-momentum $\boldsymbol{p}_N$ from its motion inside the nucleus

$$s_{\text{eff}} = (P_\gamma + P_N)^2. \tag{1}$$

The nucleon momentum $\boldsymbol{p}_N$ is obtained in the factorization approximation [3] from the momentum transfer $\boldsymbol{q}$ to

the nucleus by

$$\boldsymbol{p}_N = -\frac{A-1}{2A}\boldsymbol{q} = -\frac{3}{7}\boldsymbol{q}, \qquad (2)$$

where A is the nuclear mass number and all momenta are in the laboratory frame (note that the expressions in [3] refer to the center-of-momentum frame). The amplitudes of the elementary reactions are then evaluated at $W(E_\gamma, \boldsymbol{q})$.

The amplitude for meson photoproduction off nuclei is in general given by

$$\mathcal{F} = L + i\sigma K, \qquad \mathrm{d}\sigma = |L|^2 + |K|^2, \qquad (3)$$

with the spin-independent part L and the spin-dependent part K. It is efficiently evaluated in the CGLN parameterization [34], involving the four invariant amplitudes $F_1, \ldots, F_4$.

The simplest case is coherent π^0 production from spin $J = 0$ nuclei in the Δ-resonance region [3]. The elementary production amplitudes are identical for protons and neutrons. The dominant contribution to $\gamma A \to \pi^0 A$ for spin $J = 0$ nuclei thus involves the spin/isospin-independent part of the production amplitude. In the CGLN representation a spin-independent piece arises only from the term with the F_2 amplitude. Due to the pseudoscalar nature of the pion and the overall symmetry of the problem, this term has a $\sin(\Theta_\pi^\star)$ factor ($\Theta_\pi^\star$: pion polar angle in photon-nucleus cm system) in the amplitude [3]. Since the dominant excitation of the Δ-resonance is not isospin dependent, all amplitudes from protons and neutrons add coherently, which is reflected in a factor A in the amplitude. The full evaluation of the L piece gives

$$\frac{\mathrm{d}\sigma_0}{\mathrm{d}\Omega} = \frac{1}{2}\frac{q_\pi^\star}{k_\gamma^\star}|F_2(W)|^2 A^2 \sin^2(\Theta_\pi^\star) F_{C*}^2(q^2), \qquad (4)$$

where the ratio of pion and photon momenta $q_\pi^\star$, $k_\gamma^\star$ gives the phase-space factor for the photon-nucleus system. Numerical values for the CGLN amplitude F_2 were taken from the MAID analysis of pion photoproduction [35].

The ^{7}Li case is complicated by the unpaired proton in the $1p_{3/2}$ orbit, which gives rise to additional contributions involving also spin-flip amplitudes that may contribute to all four CGLN amplitudes. Apart from elastic reactions, the $1p_{3/2}$ proton may be excited to the $1p_{1/2}$ orbit, populating the low lying $1/2^-$ state of ^{7}Li with an excitation energy of $478\,\mathrm{keV}$. Incoherent pion production to this final state cannot be separated experimentally from the coherent process and is thus included in the measured cross sections. The spin-dependent contribution must be small compared to the spin-independent contribution because it is lacking the A^2 factor, but it is important for extreme forward or backward angles (because it has a $\cos^2(\Theta_\pi^\star)$ dependence instead of the $\sin^2(\Theta_\pi^\star)$ for the spin-independent part). These contributions are approximated from the leading M_{1+} multipole. Evaluation of the multipole expansion of the CGLN amplitudes for the spin-dependent part of the cross section leads to

$$\frac{\mathrm{d}\sigma_{sf}}{\mathrm{d}\Omega} \approx \frac{q_\pi^\star}{k_\gamma^\star}|M_{1+}(W)|^2 \cos^2(\Theta_\pi^\star)\left(F_{C*}^2(q^2) + F_{Cx*}^2(q^2)\right), \qquad (5)$$

when all multipoles except the leading M_{1+} are neglected. The incoherent excitation of the nucleus is included, but the contribution turns out to be negligible (see sect. 5.1). The amplitudes M_{1+} are again taken from the MAID-model [35]. For the full PWIA cross section the incoherent sum,

$$\frac{\mathrm{d}\sigma_{\pi A}}{\mathrm{d}\Omega} = \frac{\mathrm{d}\sigma_0}{\mathrm{d}\Omega} + \frac{\mathrm{d}\sigma_{sf}}{\mathrm{d}\Omega}, \qquad (6)$$

is used.

The situation is different for η production. Since the elementary reaction is completely dominated by an isovector, spin-flip amplitude, there is no piece corresponding to eq. (4) in pion production. Like in the ^{3}He case [10], the main contribution to coherent production comes from the S_{11} excitation of the unpaired nucleon via a spin-flip transition. The main difference is that ^{3}He has an unpaired neutron while ^{7}Li has an unpaired proton. We use therefore a similar PWIA as for ^{3}He in [10], including the incoherent excitation via the F_{Cx*} term,

$$\frac{\mathrm{d}\sigma_{\eta A}}{\mathrm{d}\Omega} = \left(\frac{q_\eta^{(A)}}{k_\gamma^{(A)}}\frac{k_\gamma^{(N)}}{q_\eta^{(N)}}\right)\frac{\mathrm{d}\sigma_{\mathrm{elem}}}{\mathrm{d}\Omega}\left(F_{C*}^2(q^2) + F_{Cx*}^2(q^2)\right), \qquad (7)$$

with a parameterization of the measured $\gamma p \to p\eta$ cross section from [36] for the elementary cross section $\mathrm{d}\sigma_{\mathrm{elem}}$. The change of phase space between the different cm systems is derived from the photon and η three-momenta in the photon-nucleon ($k_\gamma^{(N)}$, $q_\eta^{(N)}$), and photon-nucleus ($k_\gamma^{(A)}$, $q_\eta^{(A)}$) cm systems.

3 Experimental setup

The experimental setup was identical to the one used in [37,38], apart from the target (liquid-hydrogen targets for [37,38], threshold settings, and trigger conditions.

The measurement used the tagged photon beam [39, 40] from a primary 883 MeV electron beam of the Mainz MAMI accelerator [41,42]. The photons irradiated a ^{7}Li target (enrichment 99%) of 5.4 cm length and a density of $0.534\,\mathrm{g/cm}^3$, corresponding to a surface density of 0.264 nuclei/barn. The reaction products were detected with an electromagnetic calorimeter composed of the Crystal Ball (CB) [43] and TAPS detectors [44,45]. The 672 NaI crystals of the CB covered the full azimuthal angle for polar angles between $20°$ and $160°$ around the target, which was mounted in the center of the CB. TAPS covered polar angles between $1°$ and $20°$ as a hexagonal wall of 510 BaF$_2$ crystals, mounted 1.75 m downstream from the target. Individual plastic detectors in front of each crystal were used for charged particle identification. A schematic view of the setup, which covered $\approx 98\%$ of 4π, is shown in fig. 3. It was complemented by a cylindrical Particle Identification Detector (PID) [46], mounted around the target inside the CB, which covered the same solid angle as the CB.

The experiment trigger was based on a subdivision of the CB and TAPS into logical sectors. For TAPS these
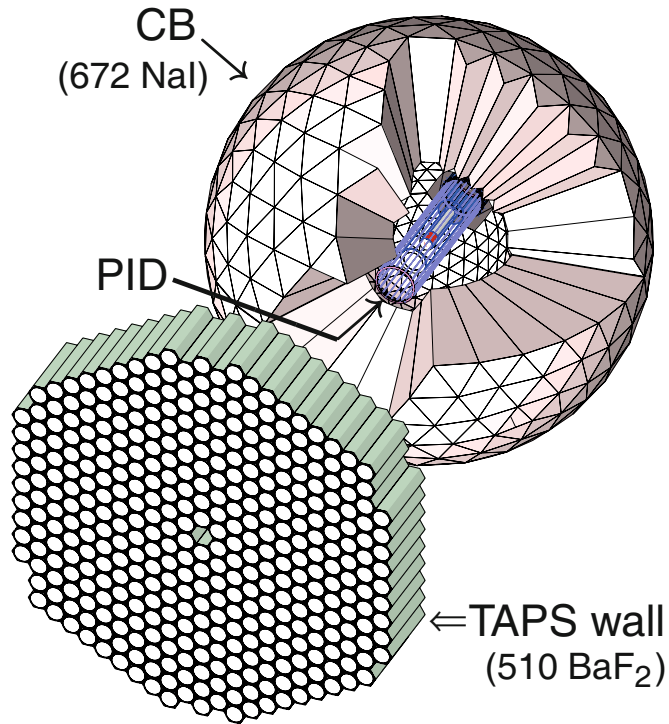
Fig. 3. Setup of the electromagnetic calorimeter combining the Crystal Ball and TAPS detectors. Detectors for charged particle identification were mounted in the Crystal Ball (PID and MWPC) and in front of the TAPS forward wall (TAPS Veto-detector).

were eight sectors of 64 modules in a pizza-like geometry, and for the CB 45 rectangles. The trigger required signals in at least two logical sectors of the calorimeter above a threshold of 20 MeV and an analog energy sum of the CB modules above 50 MeV. Once a valid trigger had been generated, thresholds for the readout of individual modules were 5 MeV in TAPS and 2 MeV in the CB.

4 Data analysis

The different analysis steps for the identification of photons, charged pions, and recoil nucleons are discussed in more detail in [37,38]. The analysis of coherent neutral meson production off nuclei is special in so far as no charged particles (no charged pions, no recoil protons) may occur in the final state. Detection of charged particles was only used to veto events, which simplifies the analysis (there was no need to separate charged pions from protons or to extract energy information for the charged particles). Accepted were only events with exactly two photons (from the $\pi^0 \to \gamma\gamma$ or $\eta \to \gamma\gamma$ decays) or with exactly six photons ($\eta \to 3\pi^0 \to 6\gamma$). These are particularly clean data samples.

The invariant-mass spectrum of photon pairs for incident photon energies below 300 MeV is shown in fig. 4. It is practically background free. No other reactions with significant cross section produce two or more photons in this energy range.
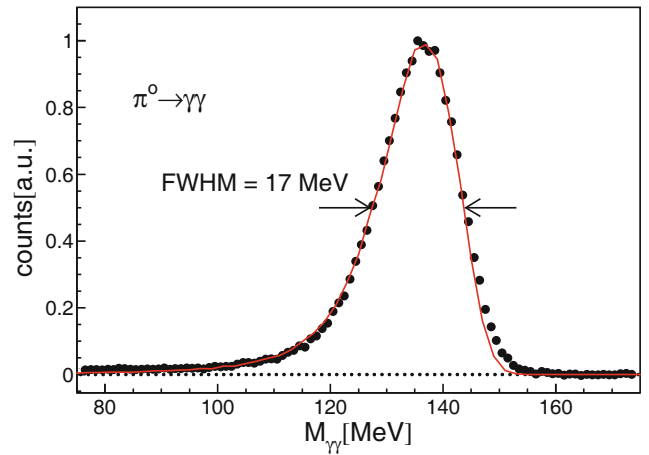

Fig. 4. Invariant-mass spectrum for two-photon events for incident photon energies below 300 MeV. Statistical uncertainties smaller than symbol sizes. The solid (red) curve is a Monte Carlo simulation of the detector response.

Double π^0 production sets in with a very low cross section around 300 MeV and loss of two of the four decay photons is unlikely. The only possible background source is production of single π^0 off quasi-free neutrons with loss of one decay photon and misidentification of the neutron as photon. However, the corresponding recoil neutrons are mostly emitted to forward angles and can be identified in TAPS with time of flight *versus* energy and pulse-shape analyses. The important step is then the separation of the coherent reaction from breakup reactions with emission of recoil nucleons. The suppression of such events by the required non-detection of recoil nucleons is limited since the detection efficiency for recoil neutrons is only on the order of 30% (larger than 90% for recoil protons). We use therefore in addition the overdetermination of the reaction kinematics of the two-body final state. The laboratory kinetic energy of the meson E_m^{lab} is directly measured with the calorimeter, and its kinetic cm energy $E_m^\star$ follows from the incident photon energy E_γ.

The mesons are boosted into the cm system and the difference ΔE_π of the two kinetic energies in the cm system is constructed as

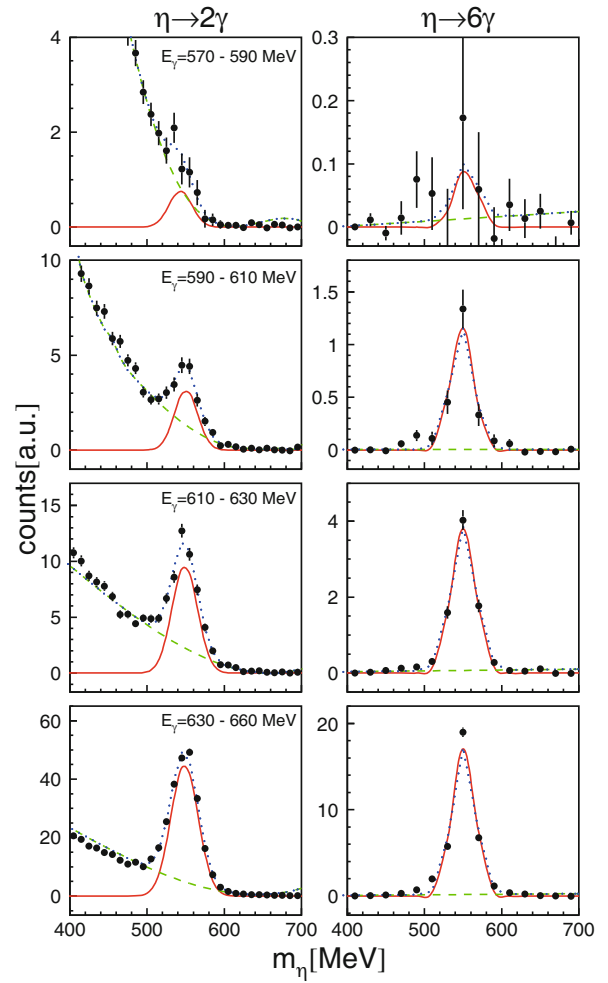$$\Delta E_m = E_m^\star(E_m^{\mathrm{lab}}) - E_m^\star(E_\gamma). \qquad (8)$$

The result of this analysis for pion production is shown in fig. 5. The peaks at zero missing energy correspond to coherent production and dominate the process at low incident photon energies. At higher incident photon energies breakup background appears at negative missing energies. The shape of the signals was generated with a full Monte Carlo simulation of the experiment using the GEANT3 package [47]. The event generator for the coherent process was based on trivial two-body kinematics; for the breakup reaction, the momentum distribution of the bound nucleons was taken into account. Final-state interactions were not taken into account, which explains the deviations between data and Monte Carlo in the tails of
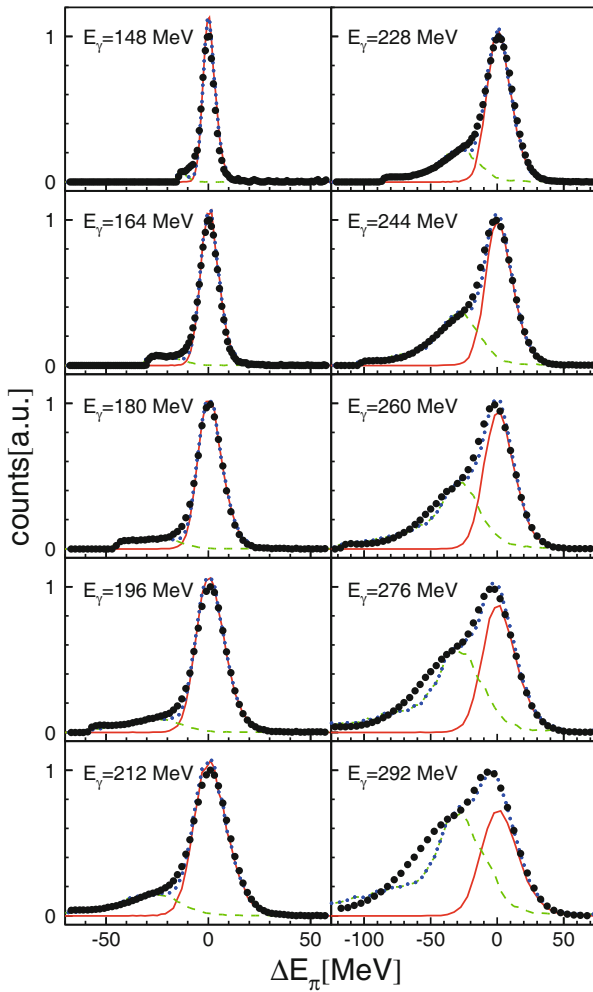
Fig. 5. Missing-energy analysis for single π^0 production for different incident photon energies. Black dots: measurement (statistical uncertainties smaller than symbol size). Solid (red) curves: MC simulation for coherent events. Dashed (green) curves: MC for breakup events. Dotted (blue): sum of both.

Fig. 6. Invariant-mass spectra for two-photon (left-hand side) and six-photon (right-hand side) events in the energy region of the η production threshold. Solid (red) lines: signal shapes. Dashed (green) lines: fitted background. Dotted (blue) curves: sum of both. Ranges of incident photon energies are given on the left-hand side.

the distributions for higher incident photon energies. The separation of coherent and breakup processes, which must be done in dependence on the pion angles, is straightforward for the energy range up to $E_\gamma = 300$ MeV as shown in fig. 5. At higher incident photon energies, the contribution from breakup reactions becomes dominant in the angle-integrated missing-energy spectra. Across the angular distribution missing energy spectra vary. The fraction of coherent events compared to breakup is larger for forward angles, but due to kinematics the separation between coherent and breakup events in missing energy is better at backward angles. The "coherent reaction" includes incoherent excitation of the 478 keV level, which cannot be resolved by the missing-energy analysis.

The analysis for coherent η production follows the same scheme. Invariant-mass and missing-energy spectra are summarized in figs. 6 and 7. The main difference to π^0 production is that, near threshold, the ratio of coherent to breakup cross sections is much less favorable. This

comes from two effects discussed in sect. 2. The involved momentum transfers are much larger, suppressing the coherent cross section via the form factor. Since furthermore (apart from small components in the nuclear wave functions) only the $1p_{3/2}$ proton contributes, the A^2 factor is missing in the coherent cross section.

The invariant-mass peaks from the two-photon decays show some background (double π^0 production with two undetected photons, single π^0 production off quasi-free neutrons with one undetected photon and a misidentified neutron), which must be subtracted. The invariant-mass signals of the six-photon decays are much cleaner. In this case, the invariant masses of the three π^0-mesons are also used to identify the reaction as discussed in [10]. The contribution of breakup background to the missing-energy spectra is substantial. A clean coherent signal appears only in the immediate threshold region. At higher energies the signal can be extracted only by fitting the
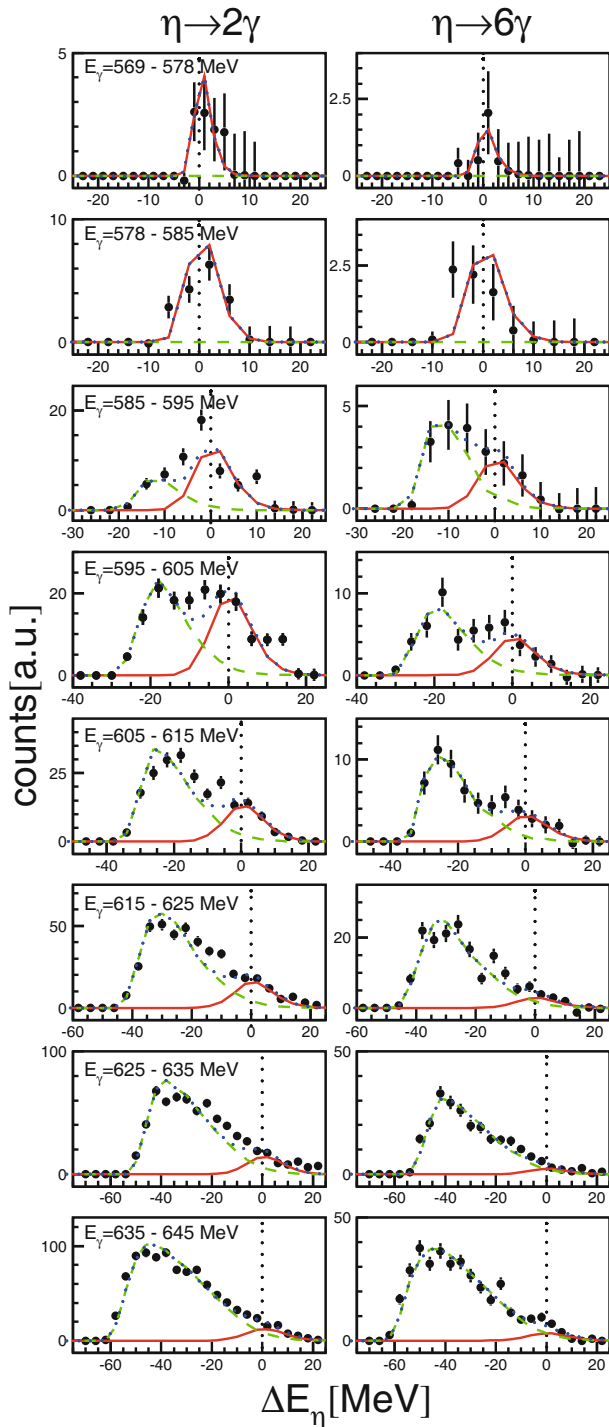
Fig. 7. Missing-energy spectra for events in the η invariant-mass peaks for different ranges of incident photon energy. Notation for curves is as in fig. 4. Vertical dotted lines: expected positions of coherent peaks. Left-hand side: two-photon events. Right-hand side: six-photon events.

simulated line shapes to the data, which for incident photon energies above 650 MeV becomes unfeasible. However, the simultaneous extraction of the cross section from the two different η-decay channels gives some estimate for the typical level of uncertainty.

Absolute cross sections were extracted from the measured yields with the target surface density, the incident photon flux, and the simulated detection efficiencies. The latter were generated with GEANT3 [47] simulations. Typical values (depending on the incident photon energy and polar angle of the meson) are 20%–50% for coherent π^0 production and 35%–40% for coherent η production to the six-photon final state and 60%–70% for the two-photon final state. The uncertainty for the detection efficiency simulations is smaller than in [38] for two reasons. Only photons had to be detected, for which the response of the detector system is best understood. There is no additional uncertainty from the properties of the event generator because in both cases only trivial two-body kinematics is involved in the final state. We estimate the systematic uncertainty of the detection efficiency below the 5% level. The incident photon flux was determined from the counting of the number of deflected electrons in the focal plane by live-time gated scalers. The fraction of correlated photons that pass the collimator and reach the target (tagging efficiency, $\approx 50\%$ for this experiment) was determined with special experimental runs. A total absorbing lead-glass counter was moved into the photon beam at reduced intensity of the primary electron beam. The intensity was reduced at the electron source, so that no accelerator parameters differed from normal running. In addition to these periodical absolute measurements the intensity was monitored in arbitrary units during normal data taking with an inonization chamber at the end of the photon-beam line. The systematic uncertainty for the flux measurement is estimated below the 5% level. The systematic uncertainty of the surface density of the solid ^{7}Li target is estimated as 3% (due to a somewhat irregular shape of the target).

The largest uncertainty is related to the separation of coherent signal and breakup background. For coherent π^0 production we estimate a systematic uncertainty due to this effect of 2%–5% for incident photon energies from threshold to 200 MeV, 5%–8% between 200 MeV and 300 MeV, and 8%–20% between 300 MeV and 500 MeV. For η production most of this uncertainty is reflected in the statistical uncertainties of the yields, which include the uncertainty related to the fitting of the missing-energy spectra.

5 Results

The results for the two reaction channels are of different quality and intended for different purposes. The π^0 data have excellent statistical quality. In most figures their statistical error bars are smaller than the symbol sizes. Although we compare them here only to PWIA approximations to discuss their most important features, they may serve as precision tests for more advanced models, taking into account the correct nuclear structure of ^{7}Li and the nuclear effects beyond PWIA.

The pioneering results for η production, at a cross section level of 10–20 nb, have limited statistical precision, but still allow a comparison of the threshold behavior to the ^{3}He case.
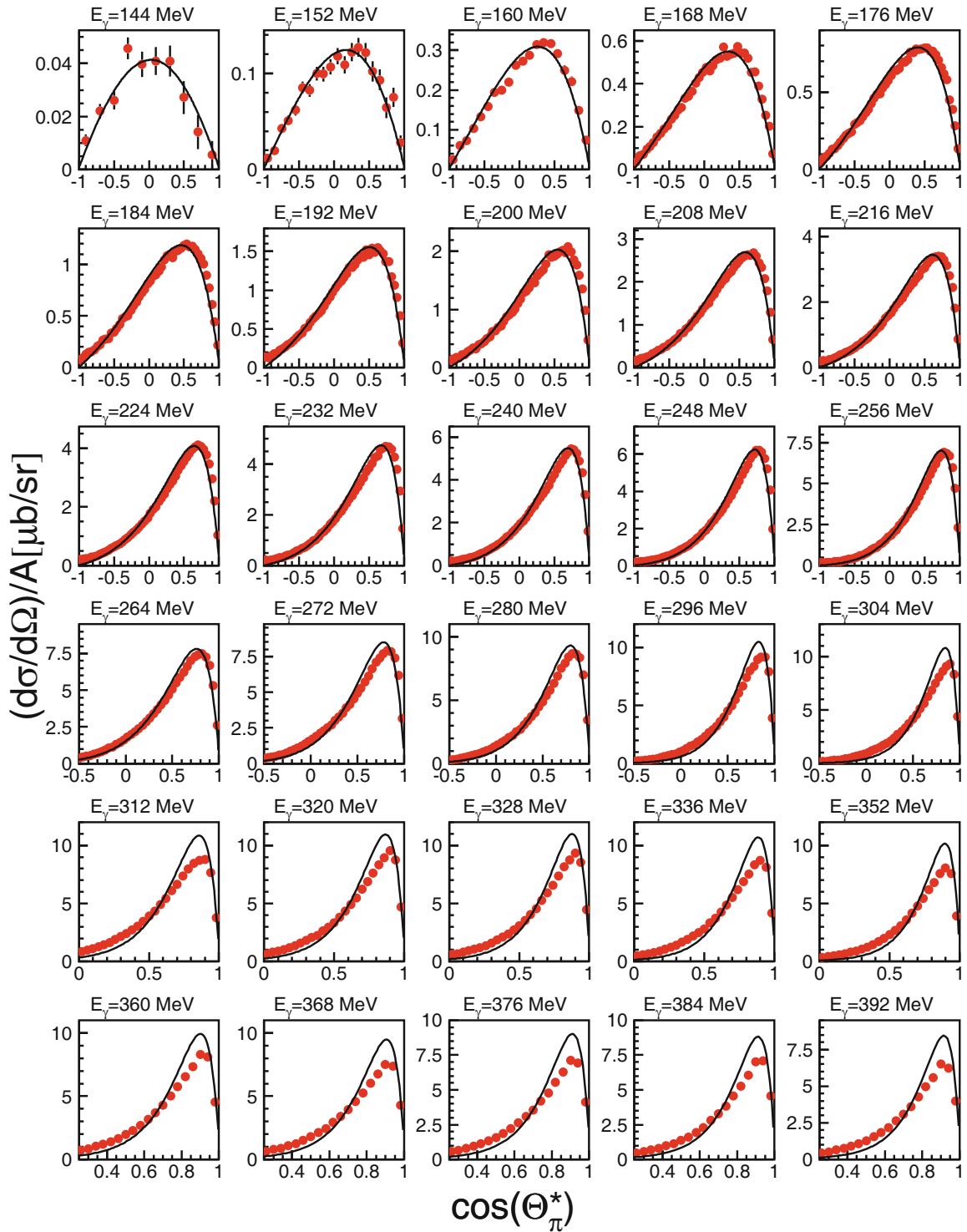
Fig. 8. Angular distributions for coherent π^0 production for different ranges of incident photon energy. Curves: results of PWIA model normalized in absolute scale to experiment.

5.1 Coherent π^0 photoproduction

Angular distributions and the total cross section for the $\gamma + {}^7\mathrm{Li} \rightarrow {}^7\mathrm{Li} + \pi^0$ reaction are summarized in figs. 8 and 9. We discuss first the total cross section. The energy dependence and absolute magnitude reflect the properties of the elementary production cross section off the nucleon, trivial factors like A^2 and $\sin^2(\Theta_\pi^\star)$, the nuclear form fac-

tor, FSI effects, and possible in-medium modifications of the involved nucleon resonances (here the $\Delta(1232)$). We compare the data to similar results for the deuteron [48] and ${}^{12}\mathrm{C}$ [4]. The systematic evolution of the Δ-resonance peak depending on the nuclear mass number from "almost free" production for the deuteron to "almost nuclear density" for carbon is clearly visible.
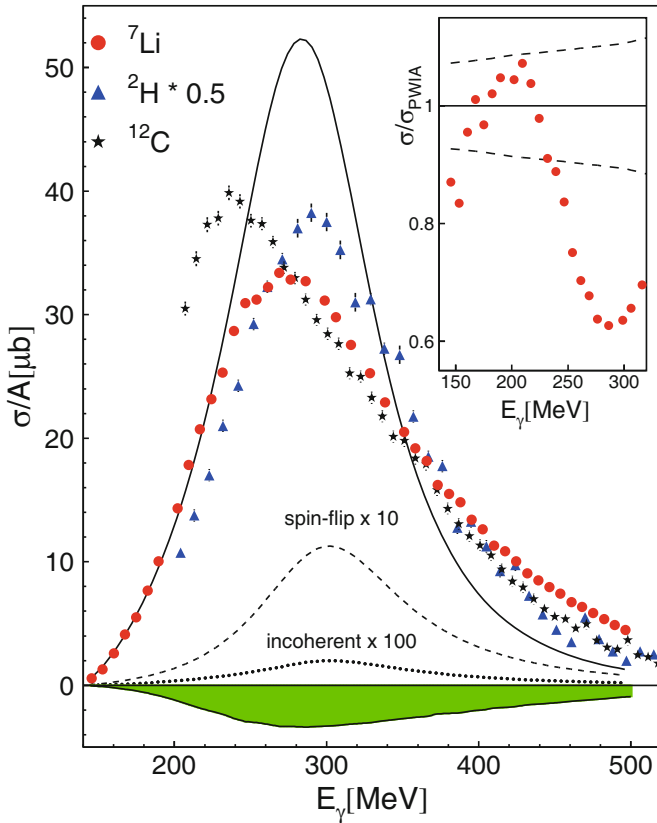
Fig. 9. Total cross section for coherent π^0 production. The shaded (green) band indicates the size of systematic uncertainty of the data. Data for the deuteron (scaled down by factor of two) [48] and ^{12}C [4] for comparison. Solid curve: PWIA results, eq. (6). Dashed curve: predicted contribution of spin-flip amplitude (first term of eq. (5)) scaled up by a factor of 10. Dotted curve: incoherent contribution from excitation of 478 keV level (second term of eq. (5)) scaled up by factor of 100. Insert: ratio of measured cross section and PWIA. Dashed lines: range of systematic uncertainty of ^{7}Li data.

One should keep in mind, as discussed in detail in [4], that the effective position of the Δ-resonance peak is determined by different effects: the interplay between the nuclear form factor and the $\sin^2(\Theta)$ term in the PWIA approximation (see eq. (4); not valid for the $J = 1$ deuteron which is lacking the $\sin^2$ term), the FSI effects in distorted-wave impulse approximation (DWIA), and the density-dependent in-medium modification of the position and width of the resonance. Actually, the model of Drechsel *et al.* [3], which reproduced quite well the data for nuclei from carbon to lead [4], predicts an *upward* shift of the $\Delta(1232)$ in-medium resonance position; although the peak in the cross section appears to be *downward* shifted due to the other effects. The lithium case is interesting because it is transitional between the Δ-in-vacuum and Δ-in-normally-dense-matter cases. Previous results [4] have shown that the measured cross sections from carbon to lead can be reproduced with Δ self-energies extracted from ^{4}He data. However, ^{4}He is itself a very dense nucleus and the effective density of ^{7}Li is significantly lower than for any of

the nuclei studied so far. The extraction of Δ self-energies from the lithium data will require detailed model calculations, taking into account the FSI effects, which are not yet available but in progress.

Here, we compare the measured cross sections to the PWIA modeling discussed in sect. 2. It is obvious from the figure that the elastic spin-flip term (term with F_{C*}^2 in eq. (5)) and the incoherent excitation of the 478 keV state of the ^{7}Li nucleus (term with F_{Cx*}^2 in eq. (5)) are negligible effects for the total cross section, both much smaller than the systematic uncertainty of the data. (Note, however, the importance of the spin-flip term for the angular distributions discussed below.) In the low-energy range, up to incident photon energies of ≈ 225 MeV, the measured cross sections agree surprisingly well with the PWIA results (mostly within systematic uncertainties of the data). This demonstrates that the trivial effects of the coherent process are well understood in PWIA and that in this regime effects from FSI and in-medium modifications of the Δ-resonance must be either both small or cancelling. In the maximum of the Δ-resonance, PWIA largely overestimates the data. This is consistent with the expected onset of strong FSI and the in-medium damping of the Δ-resonance. At even higher incident photon energies, beyond the energy range where the elementary cross section is dominated by the $\Delta(1232)$ excitation, the model is missing contributions from other photoproduction multipoles (*e.g.*, from the excitation of the $P_{11}(1440)$ and $D_{13}(1520)$ resonances and background terms), so that no agreement can be expected.

The shape of the angular distributions in fig. 8 is quite well reproduced at low incident photon energies and even reasonably well at higher energies. This is so, because the shape is dominated by the $\sin^2(\Theta)$ term and the nuclear form factor. However, a closer inspection of the angular distributions also shows some systematic deviations between experiment and PWIA for the energy range where FSI effects seem to be small. For a more detailed analysis, fig. 10 shows a reduced version of the differential cross sections as a function of the squared momentum transfer q^2. The cross sections have been divided by the PWIA estimate from eq. (6), but without the form factor terms in eqs. (4) and (5). The square roots of these ratios, shown in the figure, correspond to the nuclear mass form factor when the PWIA is valid (and the incoherent excitation can be neglected). Shown are only the results for pion cm-angles with $\cos(\Theta_\pi^\star) > -0.5$, where the PWIA approach seems to be reasonable. The first important observation is that the q^2 dependence of these distributions is almost independent of incident photon energy. This is what one would expect for a q^2 dependence related to the nuclear form factor.

It was then tested whether the data can be fitted with a model of the form factor. The form corresponding to a simple harmonic oscillator shell model,

$$F_{HO}(q^2) = d(1 - cq^2) \exp(-aq^2), \qquad (9)$$

did not give satisfying results for the whole range of momentum transfers (see below). Much better results were
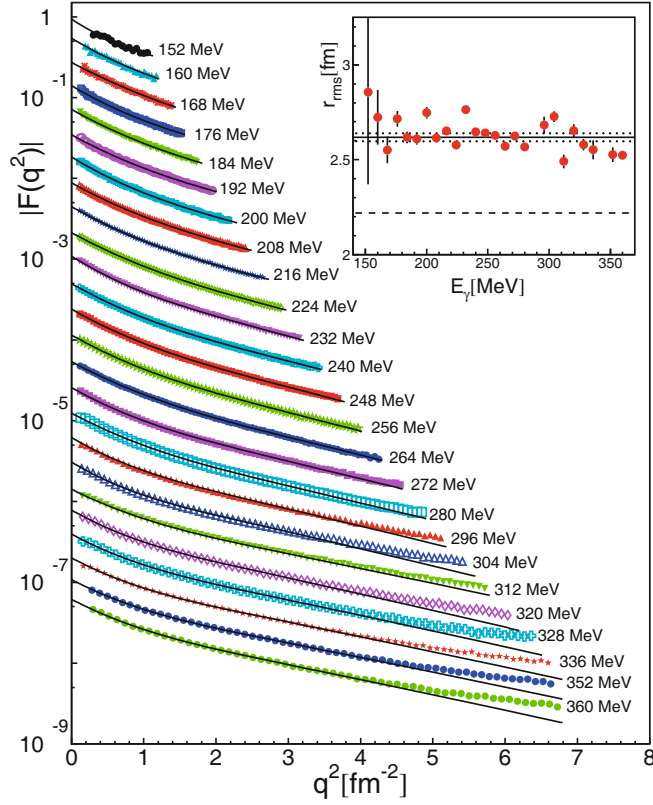
Fig. 10. Form factor of ^{7}Li extracted from the ratio of measured angular distributions and PWIA results for different ranges of incident photon energy (see text). The absolute scale corresponds to the 152 MeV data, the other data are scaled down by successive factors of two. The solid lines correspond to fits with eq. (10). The insert shows the rms mass radii (red dots) extracted from the fits with eq. (12). The solid line represents the average (dotted lines statistical uncertainty), the dashed line the rms charge radius (for point-like protons).

Fig. 11. Average of the form factors from fig. 10 compared to the charge form factors from electron scattering (divided by proton charge form factor). Solid (blue) line: fit to present data ($q^2 < 3$ fm^{-2}) with eq. (10). Results for fit with eq. (16) and $N = 5$ ($q^2 < 3$ fm^{-2}), and fit with $N = 3$ for $q^2 < 0.5$ fm^{-2} (dashed and dotted lines) are not distinguishable from solid line. (Black) solid line: fit of electron scattering data with eq. (10).

obtained with the double-well form for s- and p-orbits used in [29],
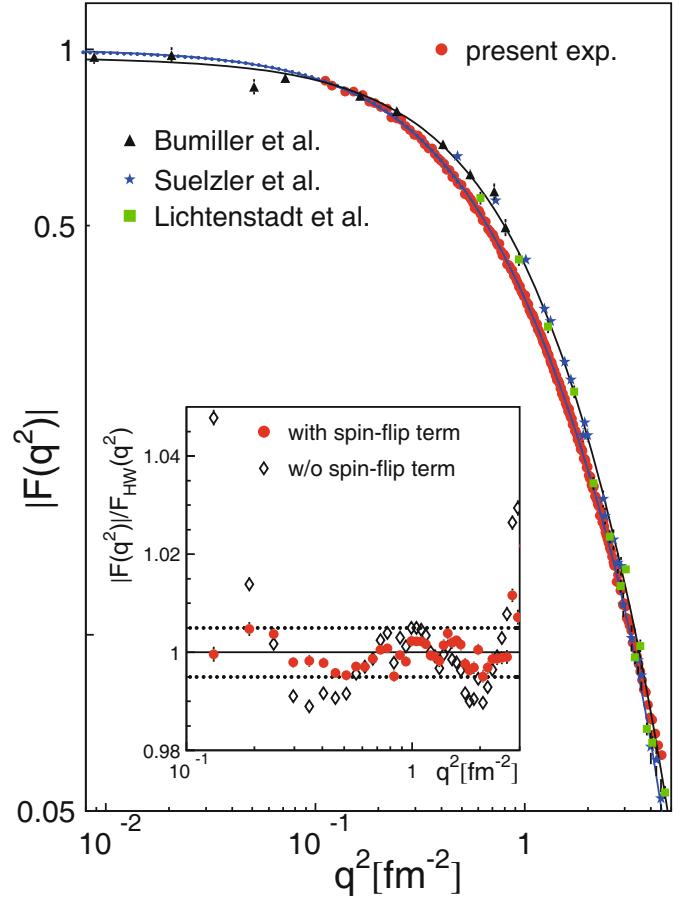
$$
\begin{aligned}
F_{MO} = a_0 &\left[\frac{2}{3} \exp(-q^2 b_1^2/4) \right. \\
&\left. + \frac{1}{3}(1 - q^2 a_2^2/6) \exp(-q^2 b_2^2/4) \right] \\
b_i^2 = a_i^2(1 - 1/A), \quad &i = 1, 2, \tag{10}
\end{aligned}
$$

where a_0 accounts for the overall normalization and a_1, a_2 are the well-strength parameters of the s- and p-wells. Fits with this model form factor are shown in fig. 10 as solid lines. They excellently describe the data over a large range of incident photon energies and momentum transfers with almost identical parameters. The average values of the well-strength parameters are

$$
\begin{aligned}
a_1 &= (1.599 \pm 0.001) \text{ fm}, \\
a_2 &= (2.47 \pm 0.06) \text{ fm}. \tag{11}
\end{aligned}
$$

Suelzle *et al.* [29] quote for the charge distribution parameters $a_1 = (1.55 \pm 0.015)$ fm and $a_2 = (2.02 \pm 0.06)$ fm so

that the s-well strength is very similar for charge and mass distribution (3% difference), while the p-well strength is $\approx 20\%$ larger for the mass distribution. The rms radius is related to these parameters by

$$
r_{rms}^2 = \frac{A-1}{A}\left(a_1^2 + \frac{1}{2}a_2^2\right) + \frac{1}{3}a_2^2. \tag{12}
$$

The values for r_{rms} obtained from the fits are shown in the insert of fig. 10. They show no systematic variation with incident photon energy and their average of ≈ 2.62 fm is significantly larger than the r_{rms} radius of the charge distribution (≈ 2.27 fm in [29]; note that the value of 2.43 fm quoted in this reference includes the charge radius of the proton).

For a more detailed analysis the average of the distributions from fig. 10 for incident photon energies up to 280 MeV (after renormalization of their absolute scales) is compared in fig. 11 to the charge form factor values from [29,31,32]. It is evident that the q^2 dependence of

Table 1. Fit results for the mass rms radius. Results are given in column 1 for fits with the full PWIA model (eqs. (4)–(6)), in column 2 for a truncated model without the spin-flip contribution (eq. (5)), and in column 3 for a model with the spin-flip contribution arbitrarily doubled. Column 4 shows for comparison results of fits to charge form factor from electron scattering (divided by proton charge form factor). First row [1] average of the fit results from fig. 10 with the double-well model (eq. (10)) over an range of incident photon energies from 150 MeV–360 MeV (χ^2 values are averages for all fits). Second row [2] fit with the double-well model to the averaged form factor for $q^2 < 3\,\mathrm{fm}^{-2}$ (fig. 11). Third row [3] fit with series (eq. (16) with $N = 5$ (for the model with neglected spin-flip term with $N = 7$, since $N = 5$ did not converge). Fourth row [4] fit with series with $N = 2$ for $q^2 < 0.5\,\mathrm{fm}^{-2}$ (only few data for charge form factor).

Method	Full model		No spin-flip		Spin-flip doubled		Charge form factor	
	$r_{rms}^{(m)}$ [fm]	χ^2	$r_{rms}^{(m)}$ [fm]	χ^2	$r_{rms}^{(m)}$ [fm]	χ^2	$r_{rms}^{(ch)}$ [fm]	χ^2
[1] Double well	2.618±0.004	3.4	2.710±0.004	7.2	2.587±0.004	3.2	–	–
[2] Double well	2.659±0.007	8.6	2.898±0.003	24	2.612±0.002	8.4	2.30±0.02	3.7
[3] Series $N = 5$ (7)	2.635±0.002	8.4	2.981±0.002	16	2.575±0.002	8.3	2.17±0.04	1.9
[4] Series $N = 2$ ($q^2 < 0.5\,\mathrm{fm}^{-2}$)	2.56±0.12	5.9	3.12±0.08	14	2.398±0.15	7.2	2.2±1.2	1.2

the electron scattering data is different from the present results. Both data sets have been fitted for the range of $q^2 < 3\,\mathrm{fm}^{-2}$ with eqs. (9) and (10). The fits with the simple harmonic oscillator model (eq. (9)) were of much inferior quality (reduced $\chi^2 \approx 880$ for present data compared to ≈ 8 for the double-well form eq. (10)) and were not further considered. The fits with the double-well form from eq. (10) are shown in fig. 11 as solid blue (present data) and solid black (electron scattering data) lines. They correspond to the following rms radii ($r_{rms}^{(ch)}$: electron data; $r_{rms}^{(m)}$: present data),

$$r_{rms}^{(ch)} = (2.30 \pm 0.02)\,\mathrm{fm}, \qquad (13)$$
$$r_{rms}^{(m)} = (2.66 \pm 0.01)\,\mathrm{fm}. \qquad (14)$$

The insert of fig. 11 shows the ratio of the present data and this fit (filled, red points). For q^2-values up to $3\,\mathrm{fm}^{-2}$ the fit reproduces the shape to within $\pm 0.5\%$. Due to this small systematic differences between fit curve and data, the result for the radius is almost independent of the fitted range. If, for example, we fit only the data for incident photon energies below 225 MeV, where agreement between data and PWIA is best, the radius changes only from 2.659 fm to 2.653 fm. Also shown in the insert (black, open points) is the result from an analysis that neglected the spin-flip term (eq. (5)) in the elementary production cross section. The influence of this term is substantial at small q^2-values; the reduced χ^2 of the fit rises from 8.6 to 24 if it is omitted.

The rms radius can be also extracted from the present data without the use of a specific model for the form factor from its slope for $q^2 \rightarrow 0$, using the expansion

$$F(q^2) = 1 - \frac{q^2}{6} r_{rms}^2 + \mathcal{O}(q^4). \qquad (15)$$

The data were fitted with the ansatz

$$F(q^2) = \sum_{n=0}^{N} c_n q^{2n}, \qquad (16)$$

from which the rms radius follows as

$$r_{rms} = \sqrt{-6c_1/c_0}, \qquad (17)$$

where for correctly normalized form factors c_0 would be unity (here it differs by a few per cent from unity).

Different fits have been exploited. Two extreme cases are fits for the q^2 range up to $3\,\mathrm{fm}^{-2}$ with $N = 5$ and with $N = 2$ only for small momentum transfers ($q^2 < 0.5\,\mathrm{fm}^{-2}$). The results for $r_{rms}^{(m)}$ extracted from eq. (17) are in agreement and close to the above value from the double-well harmonic-oscillator model,

$$r_{rms}^{(m)} = (2.635 \pm 0.002)\,\mathrm{fm}, \qquad (18)$$

for the $N = 5$ fit over the full range and

$$r_{rms}^{(m)} = (2.56 \pm 0.12)\,\mathrm{fm}, \qquad (19)$$

for the slope from the low-momentum transfer $N = 2$ fit (quoted uncertainties are statistical). The fit curves are so similar to the double-well result that they are indistinguishable from it in fig. 11.

The results for all model fits are summarized in table 1. The form factors derived in PWIA from the coherent pion data correspond to an rms mass radius of $\approx (2.60–2.65)\,\mathrm{fm}^{-2}$ (column 1 of the table), which is significantly larger than the result for the charge radius (column 4 of the table). The reduced χ^2 of the fits is larger than unity, which is due to the systematic structure of the form factor at the sub-percent level (see insert of fig. 11), which is significant within statistical uncertainties, but much smaller than (energy-dependent) systematic uncertainties not included in the fitting process.

One source of systematic uncertainty is the contribution of the spin-flip term (eq. (5)) in the PWIA approximation, which includes only the dominant M_{1+} amplitude and ignores all other production multipoles. Its influence has been tested by model fits: excluding it completely (column 2 of table 1) and arbitrary doubling its strength (column 3). Excluding the spin-flip contribution

increases significantly the χ^2 of the fits and increases the value of the radius. Enhancing the spin-flip term by a factor of two is quite a large (probably unrealistic) variation, since in the Δ-resonance range it is strongly dominated by the well-known M_{1+} multipole. The χ^2-values of these fits are similar to the standard version and the radius becomes smaller, but is still larger than the charge radius. The comparison gives some indication of the possible size of systematic uncertainty due to this term.

The contribution of the inelastic 478 keV excitation was ignored for the form factor extraction. To test its importance we subtracted the PWIA estimate for this process from the measured angular distributions and repeated the analysis. This removes strength at large q^2, which makes the form factor steeper and thus tends to increase the radius. However, the effect is smaller than statistical uncertainties and can be safely neglected.

So far no model results are available for FSI effects in ^{7}Li. Results for other light nuclei (^{4}He, ^{12}C) [3,4] have shown that they are important for the energy dependence of the total cross section. Nevertheless, the good agreement of the measured total cross section with the PWIA modelling at incident photon energies below 225 MeV indicates that they must be small for ^{7}Li in this energy range. The main FSI effect depends on the pion kinetic cm energies (and thus on the incident photon energy) but it could also modify to some extent the shape of the angular distributions, which are the basis for the form factor extraction. However, the form factor fits (see insert of fig. 10) give consistent results for the mass radius $r_{rms}^{(m)}$ over a wide range of incident photon energy, over which the energy-dependent FSI effects change drastically, from a few per cent between 180 MeV and 220 MeV to almost 40% around 280 MeV (see insert of fig. 9).

In order to explain the observed difference between the extracted form factor and the charge form factor data, FSI effects with a very peculiar behavior would be needed. This is demonstrated in fig. 12, where the low-energy angular distributions are compared to a modified PWIA. The only difference to the PWIA curves in fig. 8 is that instead of the form factor from electron scattering the double-well parameterization of the present form factor data from fig. 11, corresponding to $r_{rms}^{(m)} = 2.66$ fm was used. The absolute scales of the PWIA results were renormalized to the data in order to remove the energy-dependent FSI effects. This PWIA must describe by construction the angular distributions on average. However, it actually agrees almost perfectly with the shapes of all individual distributions, with very different relations between pion angles and nuclear momentum transfers. This means that an FSI effect would be needed, which over a range of incident photon energy of more than 100 MeV has exactly the same angular and momentum-transfer dependence as a change of the form factor from an rms radius of 2.3 fm to 2.66 fm. Although this does not seem to be a likely scenario, reasonably sophisticated modelling of the FSI effects is needed before a final conclusion can be drawn. However, results for a similar analysis of coherent photoproduction off carbon, calcium, and lead nuclei
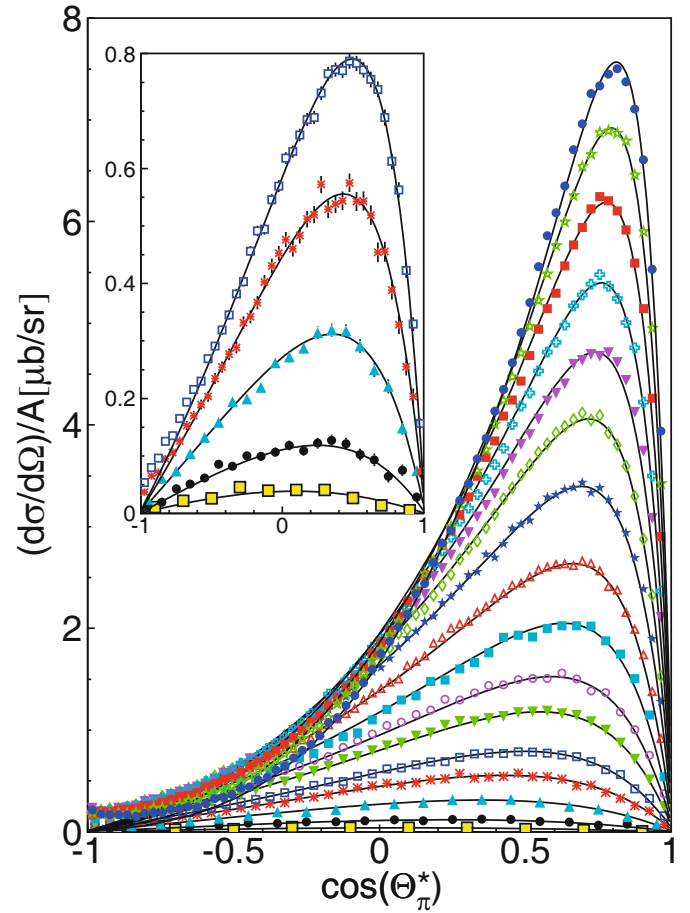

Fig. 12. Main picture: angular distributions for incident photon energies from 152 MeV (bottom curve) to 264 MeV (top curve, same energy bins as in fig. 10) compared to PWIA results using the fitted form factor. Absolute scales of model results normalized to data (see text). The insert shows on a larger scale the low-energy results (144 MeV–168 MeV).

point to a small influence of FSI on the extracted radii for light nuclei. Fully taking into account the FSI effects [5] lowered the extracted value of the mass radius for ^{208}Pb by 5.8%, for ^{40}Ca by 2.2%, but for the lighter ^{12}C only by 0.9%, while the observed difference between charge and mass radius for ^{7}Li is on the 10% level.

5.2 Coherent η photoproduction

The total cross sections extracted for the two η-decay channels, summarized in fig. 13, are nicely consistent. They show a much smoother rise at production threshold than the ^{3}He data (cf. fig. 1). For a quantitative analysis their average is compared to PWIA modelling, based on eq. (7) in fig. 14. As discussed in sect. 2 the situation is much different from the pion production since for η production the cross section is dominated by the contribution of the odd $1p_{3/2}$ proton, which is only a small correction in the π^0 case.
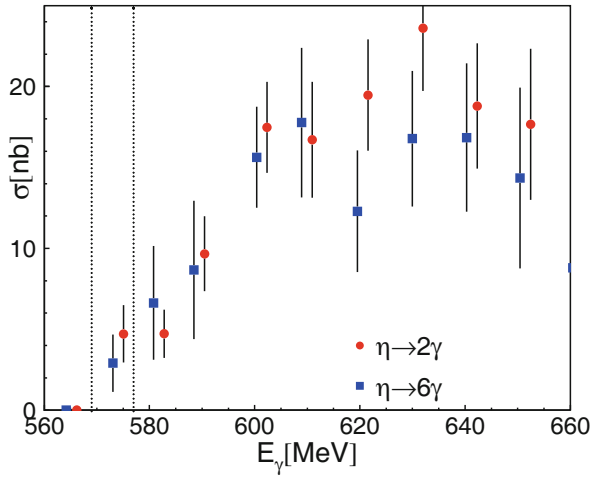
Fig. 13. Comparison of the total cross section for coherent η production from the two-photon and six-photon decay of the η. The vertical dotted lines indicate coherent and breakup thresholds.
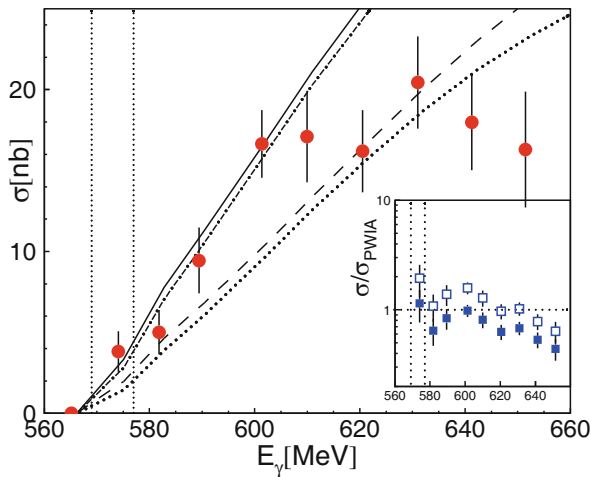
Fig. 14. Comparison of the average of the experimental two-photon and six-photon cross sections to the PWIA results. Dashed (dotted) curves: coherent contribution (eq. (7) without F_{Cx*}^2 term) based on charge form factor (mass form factor fitted to pion production). Solid (dash-dotted) curves: sum of coherent and incoherent contribution (see eq. (7)) for charge (mass form factor). The insert shows the ratio of measured cross section and PWIA results, open symbols only coherent part, filled symbols sum of coherent and incoherent contributions.

Results from PWIA, using the charge form factor or the mass form factor fitted to the pion data (dashed, respectively, dotted curves in fig. 14), are similar. This is simply so because, for η production, large-momentum transfers dominate where the two form factors agree. The relative contribution of the incoherent excitation of the 478 keV state is significant in PWIA. Also this had to be expected because for η production there is no piece with an A^2 term like eq. (4) for coherent pion production and
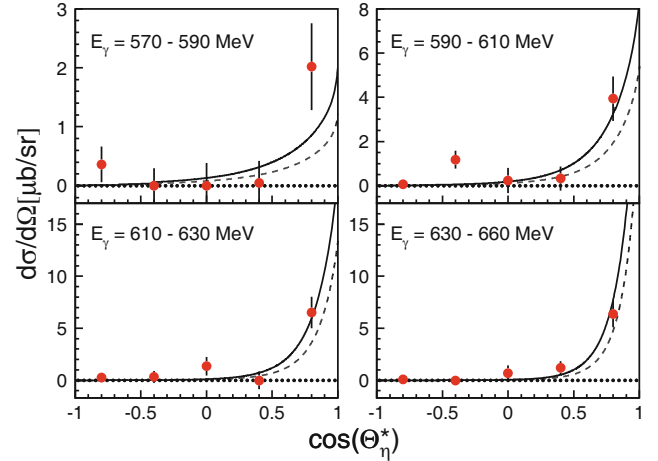
Fig. 15. Comparison of measured angular distributions for $\gamma + {}^{7}\mathrm{Li} \to {}^{7}\mathrm{Li} + \eta$ (red) dots to PWIA results. Solid lines: full PWIA. Dashed lines: only coherent part.

the elastic and inelastic form factors are similar for large-momentum transfers. The systematic uncertainty of the PWIA results is larger than in the pion case because the cross section is dominated by these less well-established contributions. However, altogether the comparison of the energy dependence of the measured total cross section and the PWIA results in fig. 14 shows no threshold enhancement above phase-space behavior, and thus no indication for the formation of a quasi-bound state. The situation is thus much different from the ${}^{3}\mathrm{He}$ case discussed in the introduction which, apart from the incoherent excitation, has similar systematic uncertainties in PWIA. Comparison of the two results highlights the special role of the η-${}^{3}\mathrm{He}$ system.

Also the results for the angular distributions, summarized in fig. 15, are consistent with this interpretation. They agree better with the momentum-transfer dependence of the form factor than in the ${}^{3}\mathrm{He}$ case and show no tendency towards isotropic behavior close to threshold.

6 Summary and conclusions

Precise data have been measured for coherent photoproduction of π^0-mesons off ${}^{7}\mathrm{Li}$ nuclei and coherent photoproduction of η-mesons off the same nucleus has been identified for the first time. The experimental results for the pion production are quite well reproduced at low incident photon energies by a PWIA dominated by the spin/isospin-independent part of the elementary production amplitude. The spin-flip amplitude from the unpaired $1p_{3/2}$ proton is considered for the leading M_{1+} multipole and the corrections applied for the incoherent excitation of the 478 keV nuclear state in ${}^{7}\mathrm{Li}$ are insignificant. This model reproduces quite well total cross sections and angular distributions at incident photon energies below 225 MeV, indicating that distortion effects from final-state interactions of the pion are small in this energy range.

After an adjustment of the nuclear form factor, which corresponds to a change in the harmonic double-well parameterization from an rms radius of 2.3 fm (reported for the charge form factor derived from electron scattering data) to 2.66 fm, the shape of angular distributions in this energy range is excellently reproduced. Exploiting the possible uncertainties due to approximations, in particular in the spin-flip term of the PWIA, we find reasonable agreement between data and PWIA for rms radii down to 2.5 fm, which are still larger than previously reported charge radii and also larger than predictions for the mass radius, which are around 2.35 fm (see *e.g.*, [7,33]). DWIA calculations with careful treatment of possible FSI effects are needed for further analysis of this discrepancy.

Coherent photoproduction of η-mesons is quite difficult to measure and so far only results for the deuteron [23, 24] and ^{3}He [9,10] had been reported. This experiment extended the mass range to ^{7}Li by measuring total cross sections on the level below 20 nb. The results, also for the angular distributions, are in good agreement with PWIA expectations and do not show an unexplained threshold enhancement as in the ^{3}He case, underlining the special role of ^{3}He as a candidate for η-mesic states.

References

1. B. Krusche, Eur. Phys. J. ST **198**, 199 (2011).
2. B. Krusche *et al.*, Eur. Phys. J. A **22**, 277 (2004).
3. D. Drechsel *et al.*, Nucl. Phys. A **660**, 423 (1999).
4. B. Krusche *et al.*, Phys. Lett. B **526**, 287 (2002).
5. B. Krusche, Eur. Phys. J. A **26**, 7 (2005).
6. C.M. Tabert *et al.*, Phys. Rev. Lett. **100**, 132301 (2008).
7. M. Tomaselli *et al.*, Phys. Rev. C **62**, 067305 (2000).
8. W. Nörtershäuser *et al.*, Phys. Rev. C **84**, 024307 (2011).
9. M. Pfeiffer *et al.*, Phys. Rev. Lett. **92**, 252001 (2004).
10. F. Pheron *et al.*, Phys. Lett. B **709**, 21 (2012).
11. B. Krusche *et al.*, Phys. Rev. Lett. **74**, 3736 (1995).
12. B. Krusche *et al.*, Phys. Lett. B **397**, 171 (1997).
13. K. Nakamura *et al.*, J. Phys. G **37**, 075021 (2010).
14. M. Röbig-Landau *et al.*, Phys. Lett. B **373**, 45 (1996).
15. T. Mertens *et al.*, Eur. Phys. J. A **38**, 195 (2008).
16. R.S. Bhalerao, L.C. Liu, Phys. Rev. Lett. **54**, 865 (1985).
17. L.C. Liu, Q. Haider, Phys. Rev. C **34**, 1845 (1986).
18. B. Mayer *et al.*, Phys. Rev. C **53**, 2068 (1996).
19. J. Smyrski *et al.*, Phys. Lett. B **649**, 258 (2007).
20. T. Mersmann *et al.*, Phys. Rev. Lett. **98**, 242301 (2007).
21. T. Rausmann *et al.*, Phys. Rev. C **80**, 017001 (2009).
22. B. Krusche *et al.*, Phys. Lett. B **358**, 40 (1995).
23. P. Hoffmann-Rothe *et al.*, Phys. Rev. Lett. **78**, 4697 (1997).
24. J. Weiss *et al.*, Eur. Phys. J. A **11**, 371 (2001).
25. J. Weiss *et al.*, Eur. Phys. J. A **16**, 275 (2003).
26. V. Hejny *et al.*, Eur. Phys. J. A **6**, 83 (1999).
27. V. Hejny *et al.*, Eur. Phys. J. A **13**, 493 (2002).
28. B. Krusche, S. Schadmand, Prog. Part. Nucl. Phys. **51**, 399 (2003).
29. L.R. Suelzle, M.R. Yearian, H. Crannell, Phys. Rev. **162**, 992 (1967).
30. J.S. McCarthy, I. Sick, R.R. Whitney, Phys. Rev. C **15**, 1396 (1977).
31. F.A. Bumiller *et al.*, Phys. Rev. C **5**, 391 (1972).
32. L. Lichtenstadt *et al.*, Phys. Lett. B **219**, 394 (1989).
33. T. Kajino *et al.*, Phys. Lett. B **202**, 475 (1988).
34. G.F. Chew, M.L. Goldberger, F.E. Low, Y. Nambu, Phys. Rev. **106**, 1345 (1957).
35. D. Drechsel, S.S. Kamalov, L. Tiator, Nucl. Phys. A **645**, 145 (1999).
36. E.F. McNicoll *et al.*, Phys. Rev. C **82**, 035208 (2010).
37. S. Schumann *et al.*, Eur. Phys. J. A **43**, 269 (2010).
38. F. Zehr *et al.*, Eur. Phys. J. A **48**, 98 (2012).
39. I. Anthony *et al.*, Nucl. Instrum. Methods A **301**, 230 (1991).
40. S.J. Hall, G.J. Miller, R. Beck, P.Jennewein, Nucl. Instrum. Methods A **368**, 698 (1996).
41. H. Herminghaus *et al.*, IEEE Trans. Nucl. Sci. **30**, 3274 (1983).
42. Th. Walcher, Prog. Part. Nucl. Phys. **24**, 189 (1990).
43. A. Starostin *et al.*, Phys. Rev. C **64**, 055205 (2001).
44. R. Novotny, IEEE Trans. Nucl. Sci. **38**, 379 (1991).
45. A.R. Gabler *et al.*, Nucl. Instrum. Methods A **346**, 168 (1994).
46. D. Watts, in *Calorimetry in Particle Physics, Proceedings of the 11th International Conference, Perugia, Italy 2004*, edited by C. Cecchi, P. Cenci, P. Lubrano, M. Pepe (World Scientific, Singapore, 2005) p. 560.
47. R. Brun *et al.*, GEANT, Cern/DD/ee/84-1 (1986).
48. B. Krusche *et al.*, Eur. Phys. J. A **6**, 309 (1999).